Proceedings of the
Annual Stability Conference
Structural Stability Research Council
Charlotte, North Carolina, April 11-14, 2023

A GBT-based finite element for the buckling analysis of thin-walled members with circular axis

Rodrigo Gonçalves[1], Nuno Peres[2], Dinar Camotim[3]

Abstract
This paper presents a GBT-based (beam) finite element for performing buckling (bifurcation) analyses of thin-walled members with circular axis. The bifurcation eigenvalue problem is obtained from the non-linear equilibrium equations, using the linear stability analysis concept, while incorporating the classic GBT kinematic assumptions, which are essential to obtain significant computational savings with respect to shell finite element models. The accuracy and efficiency of the proposed finite element is assessed in several numerical examples involving complex global-distortional-local buckling. It is shown that (i) the proposed element leads to results that match accurately those obtained with refined shell finite element models, but with much less DOFs, and (ii) the GBT modal decomposition features provide an in-depth insight into the nature of the buckling modes in curved members.

1. Introduction

It is nowadays well known that Generalized Beam Theory (GBT), a one-dimensional thin-walled beam theory accounting for cross-section in-plane and out-of-plane deformation, can handle, very accurately and efficiently, a wide range of problems involving prismatic members (see, *e.g.*, Schardt 1989, Camotim *et al*. 2010 and the list of publications at www.civil.ist.utl.pt/gbt). In particular, the fact that the member deformed configuration is described through a linear combination of hierarchic and structurally meaningful "cross-section deformation modes" renders GBT unique modal decomposition features, which enable acquiring in-depth knowledge on the mechanics of the problem under analysis.

In a recent series of papers, the authors have extended GBT to curved members with circular axis. The achievements consist in: (i) a formulation for the linear case (Peres *et al*. 2016), (ii) a procedure to determine the deformation modes for arbitrary flat-walled cross-sections (Peres *et al.* 2018), (iii) a mixed locking-free finite element (Peres *et al.* 2020), (iv) a formulation for the linear dynamic case (Peres *et al.* 2022a) and (v) a formulation for the linear stability case (Peres *et al.* 2022b). It is worth remarking that these formulations constitute consistent extensions of the standard GBT, in the sense that the same simplifying assumptions are adopted, and the deformation

[1] Associate Professor, CERIS and Universidade Nova de Lisboa, Portugal <rodrigo.goncalves@fct.unl.pt>
[2] Assistant Professor, Universidade Lusófona, Lisboa, Portugal <nuno.peres@ulusofona.pt>
[3] Full Professor, CERIS, Instituto Superior Técnico, Universidade de Lisboa, Portugal <dcamotim@civil.ist.utl.pt>

mode hierarchy follows that established in Gonçalves *et al*. (2010, 2014). It should be mentioned that the particular case of circular cross-sections (with circular axis) has been addressed by a German research group, which has presented formulations for linear, vibration and geometrically non-linear analyses (Habtemariam *et al.* 2021a, 2021b, 2022).

This paper summarizes the authors' previous work on curved members, with particular focus on the determination of the deformation modes and on the linear stability analysis case, *i.e.*, on the determination of bifurcation loads and associated buckling modes. Several numerical examples are presented to show (i) the accuracy and computational efficiency of the finite element implementation of the proposed formulation, as well as (ii) the remarkable structural insight conveyed by the GBT modal solution. For validation and comparison purposes, results obtained with refined shell finite element models are provided.

2. GBT formulation for the buckling analysis of members with circular axis

A curved thin-walled member is herein defined as shown in Fig. 1, using a global cylindrical coordinate system (θ, Z, R), with base vectors $\boldsymbol{e}_\theta$, $\boldsymbol{e}_Z$ and $\boldsymbol{e}_R$, and an axis arc-length coordinate X, defining the position of each cross-section reference point or "centre" C. In the global system, the displacement field is expressed as $\boldsymbol{U} = u_\theta \boldsymbol{e}_\theta + u_Z \boldsymbol{e}_Z + u_R \boldsymbol{e}_R$, from which the Green-Lagrange strain tensor can be obtained. The linear strain terms read

$$\begin{aligned} &\varepsilon_{\theta\theta} = \tfrac{u_R + u_{\theta,\theta}}{R}, \qquad \varepsilon_{ZZ} = u_{Z,Z}, \qquad \varepsilon_{RR} = u_{R,R}, \\ &\gamma_{\theta Z} = u_{\theta,Z} + \tfrac{u_{Z,\theta}}{R}, \quad \gamma_{\theta R} = u_{\theta,R} + \tfrac{u_{R,\theta} - u_\theta}{R}, \quad \gamma_{ZR} = u_{Z,R} + u_{R,Z}, \end{aligned} \tag{1}$$

where the commas indicate derivatives (*e.g.*, $u_{Z,Z} = \partial u_Z / \partial Z$), and the non-linear terms are

$$\begin{aligned} E_{\theta\theta}^{NL} &= \tfrac{1}{2R^2}\left(u_{Z,\theta}^2 + \left(u_R + u_{\theta,\theta}\right)^2 + \left(u_{R,\theta} - u_\theta\right)^2\right), \\ E_{ZZ}^{NL} &= \tfrac{1}{2}\left(u_{\theta,Z}^2 + u_{Z,Z}^2 + u_{R,Z}^2\right), \\ E_{RR}^{NL} &= \tfrac{1}{2}\left(u_{\theta,R}^2 + u_{Z,R}^2 + u_{R,R}^2\right), \\ 2E_{\theta Z}^{NL} &= \tfrac{1}{R}\left(u_{\theta,Z}\left(u_R + u_{\theta,\theta}\right) + u_{Z,Z}u_{Z,\theta} + u_{R,Z}\left(u_{R,\theta} - u_\theta\right)\right), \\ 2E_{\theta R}^{NL} &= \tfrac{1}{R}\left(u_{\theta,R}\left(u_R + u_{\theta,\theta}\right) + u_{Z,R}u_{Z,\theta} + u_{R,R}\left(u_{R,\theta} - u_\theta\right)\right), \\ 2E_{ZR}^{NL} &= u_{\theta,Z}u_{\theta,R} + u_{Z,Z}u_{Z,R} + u_{R,Z}u_{R,R}. \end{aligned} \tag{2}$$

Fig. 1 also shows the wall local axes (x, y, z), defining the longitudinal, wall mid-line and through-thickness directions, respectively. Using the local axes, the displacement field can be written as $\boldsymbol{U} = u\boldsymbol{e}_x + v\boldsymbol{e}_y + w\boldsymbol{e}_z$, whose components are related to the global ones through

$$u_\theta = u, \qquad u_R = v\sin\varphi + w\cos\varphi, \qquad u_Z = v\cos\varphi - w\sin\varphi \tag{3}$$

where φ is the wall angle indicated in the figure.

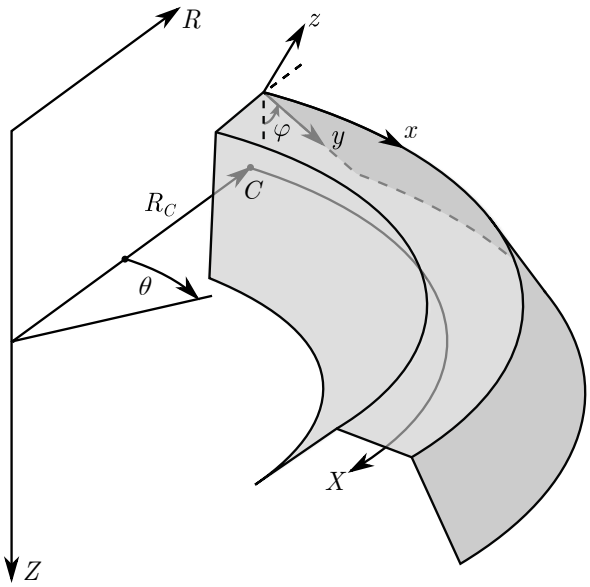

Figure 1: Global and wall (local) axes for a thin-walled beam with circular axis

A transformation to the wall local axes is performed, while (i) substituting $R = R_0 + z\cos\varphi + y\sin\varphi = \bar{R} + z\cos\varphi$ and $Z = Z_0 + y\cos\varphi - z\sin\varphi$, where point (R_0, Z_0) defines the origin of the wall local axes in the cross-section plane and $\bar{R} = R_0 + y\sin\varphi$ is the mid-line radius, (ii) enforcing Kirchhoff's thin-plate assumption ($\varepsilon_{zz} = \gamma_{\theta z} = \gamma_{yz} = 0$), (iii) keeping only terms up to linear in z, due to the thin walls, and (iv) replacing $X = R_C\theta$. This makes it possible to write the displacement field in terms of the mid-surface displacements (u^M, v^M, w) and leads to the membrane and bending linear strains

$$\begin{aligned}
\varepsilon_{xx}^M &= \overline{\beta}\left((u^M)' + K_y w - K_z v^M\right),\\
\varepsilon_{yy}^M &= v_{,y}^M,\\
\gamma_{xy}^M &= u_{,y}^M + \overline{\beta}((v^M)' + K_z u^M),\\
\varepsilon_{xx}^B &= -z\overline{\beta}\left(\overline{\beta}w'' - K_z w_{,y} - \overline{\beta}K_y K_z v^M + \overline{\beta}K_y^2 w\right),\\
\varepsilon_{yy}^B &= -z w_{,yy},\\
\gamma_{xy}^B &= -z\overline{\beta}\left(2w'_{,y} + 2\overline{\beta}K_z w' - K_y u_{,y}^M - \overline{\beta}K_y K_z u^M + \overline{\beta}K_y (v^M)'\right),
\end{aligned} \tag{4}$$

where the prime indicates a derivative with respect to X (hence $f' = \partial f/\partial X$), $K_y = \cos\varphi\,/R_C$, $K_z = -\sin\varphi\,/R_C$ and $\overline{\beta} = R_C/\overline{R}$. In thin-walled members only the membrane components of the non-linear strains need to be retained. These components read

$$\begin{aligned}
E_{xx}^{M,NL} &= \frac{\overline{\beta}^2}{2}\left(((u^M)')^2 + ((v^M)')^2 + (w')^2 + \frac{1}{R_C^2}(u^M)^2 + K_z^2(v^M)^2 + K_y^2 w^2\right.\\
&\quad \left. -2K_y K_z v^M w - 2K_z (u^M)' v^M + 2K_y (u^M)' w + 2K_z u^M (v^M)' - 2K_y u^M w'\right)\\
E_{yy}^{M,NL} &= \frac{1}{2}\left(\left(u_{,y}^M\right)^2 + \left(v_{,y}^M\right)^2 + w_{,y}^2\right),\\
2E_{xy}^{M,NL} &= \overline{\beta}\left((u^M)' u_{,y}^M + (v^M)' v_{,y}^M + w' w_{,y} - K_y u^M w_{,y} + K_y u_{,y}^M w + K_z u^M v_{,y}^M - K_z u_{,y}^M v^M\right).
\end{aligned} \tag{5}$$

Following the usual GBT procedure, the mid-surface displacements are expressed as a linear combination of pre-defined $k = 1..D$ *deformation modes* (their calculation is discussed in section 3), with components $\overline{u}_k(y), \overline{v}_k(y), \overline{w}_k(y)$, and unknown amplitude functions $\phi_k(X)$,

$$\begin{aligned} u^M &= \textstyle\sum_{k=1}^{D} \overline{u}_k(y)\phi'_k(X) = \overline{\boldsymbol{u}}^T(y)\boldsymbol{\phi}'(X), \\ v^M &= \textstyle\sum_{k=1}^{D} \overline{v}_k(y)\phi_k(X) = \overline{\boldsymbol{v}}^T(y)\boldsymbol{\phi}(X), \\ w &= \textstyle\sum_{k=1}^{D} \overline{w}_k(y)\phi_k(X) = \overline{\boldsymbol{w}}^T(y)\boldsymbol{\phi}(X), \end{aligned} \tag{6}$$

where $\overline{\boldsymbol{u}}, \overline{\boldsymbol{v}}, \overline{\boldsymbol{w}}, \boldsymbol{\phi}$ are column vectors. It is remarked that $\boldsymbol{\phi}'$ is employed in the first equation, instead of $\boldsymbol{\phi}$, to allow enforcing Vlasov's null membrane shear strain assumption ($\gamma_{xy}^M = 0$) in the small displacement case. Indeed, substituting Eqs. (6.1)-(6.2) in Eq. (4.3) a match in the amplitude functions is observed,

$$\gamma_{xy}^M = u_{,y}^M + \overline{\beta}((v^M)' + K_z u^M) = \left(\overline{\boldsymbol{u}}_{,y}^T + \overline{\beta}\overline{\boldsymbol{v}}^T + \overline{\beta}K_z\overline{\boldsymbol{u}}^T\right)\boldsymbol{\phi}', \tag{7}$$

otherwise both $\boldsymbol{\phi}$ and $\boldsymbol{\phi}'$ would appear and it would not be generally possible to enforce $\gamma_{xy}^M = 0$. Consequently, the displacement and strain fields can be written in a vector-matrix notation as

$$\boldsymbol{U} = \begin{bmatrix} U_x \\ U_y \\ U_z \end{bmatrix} = (\boldsymbol{\Xi}_{\boldsymbol{U}}^M + \boldsymbol{\Xi}_{\boldsymbol{U}}^B)\boldsymbol{\Phi}, \quad \boldsymbol{E} = \begin{bmatrix} E_{xx} \\ E_{yy} \\ 2E_{xy} \end{bmatrix} = \left(\boldsymbol{\Xi}_{\boldsymbol{\varepsilon}}^M + \boldsymbol{\Xi}_{\boldsymbol{\varepsilon}}^B + \boldsymbol{\Xi}_{\boldsymbol{E}}^{M,NL}\right)\boldsymbol{\Phi}, \tag{8}$$

with the auxiliary matrices and vectors

$$\boldsymbol{\Xi}_{\boldsymbol{U}}^M = \begin{bmatrix} \mathbf{0} & \overline{\boldsymbol{u}}^T & \mathbf{0} \\ \overline{\boldsymbol{v}}^T & \mathbf{0} & \mathbf{0} \\ \overline{\boldsymbol{w}}^T & \mathbf{0} & \mathbf{0} \end{bmatrix}, \quad \boldsymbol{\Xi}_{\boldsymbol{U}}^B = z\begin{bmatrix} \mathbf{0} & \overline{\beta}K_y\overline{\boldsymbol{u}}^T - \overline{\beta}\overline{\boldsymbol{w}}^T & \mathbf{0} \\ -\overline{\boldsymbol{w}}_{,y}^T & \mathbf{0} & \mathbf{0} \\ \mathbf{0} & \mathbf{0} & \mathbf{0} \end{bmatrix}, \quad \boldsymbol{\Phi} = \begin{bmatrix} \boldsymbol{\phi} \\ \boldsymbol{\phi}' \\ \boldsymbol{\phi}'' \end{bmatrix}. \tag{9}$$

$$\boldsymbol{\Xi}_{\boldsymbol{\varepsilon}}^{(\cdot)} = \begin{bmatrix} \left(\boldsymbol{\xi}_{11}^{(\cdot)}\right)^T & \mathbf{0} & \left(\boldsymbol{\xi}_{13}^{(\cdot)}\right)^T \\ \left(\boldsymbol{\xi}_{21}^{(\cdot)}\right)^T & \mathbf{0} & \mathbf{0} \\ \mathbf{0} & \left(\boldsymbol{\xi}_{32}^{(\cdot)}\right)^T & \mathbf{0} \end{bmatrix}, \quad \boldsymbol{\Xi}_{\boldsymbol{E}}^{M,NL} = \begin{bmatrix} \boldsymbol{\Phi}^T\boldsymbol{\Xi}_{xx}^{M,NL} \\ \boldsymbol{\Phi}^T\boldsymbol{\Xi}_{yy}^{M,NL} \\ \boldsymbol{\Phi}^T\boldsymbol{\Xi}_{xy}^{M,NL} \end{bmatrix}, \quad \boldsymbol{\Xi}_{ij}^{M,NL} = \begin{bmatrix} \boldsymbol{\xi}_{ij11} & \mathbf{0} & \mathbf{0} \\ \boldsymbol{\xi}_{ij21} & \boldsymbol{\xi}_{ij22} & \mathbf{0} \\ \boldsymbol{\xi}_{ij31} & \boldsymbol{\xi}_{ij32} & \boldsymbol{\xi}_{ij33} \end{bmatrix}, \tag{10}$$

$$\begin{aligned} \boldsymbol{\xi}_{11}^M &= \overline{\beta}\left(K_y\overline{\boldsymbol{w}} - K_z\overline{\boldsymbol{v}}\right), \\ \boldsymbol{\xi}_{13}^M &= \overline{\beta}\overline{\boldsymbol{u}}, \\ \boldsymbol{\xi}_{21}^M &= \overline{\boldsymbol{v}}_{,y}, \\ \boldsymbol{\xi}_{32}^M &= \overline{\beta}\overline{\boldsymbol{v}} + \overline{\beta}K_z\overline{\boldsymbol{u}} + \overline{\boldsymbol{u}}_{,y}, \\ \boldsymbol{\xi}_{11}^B &= -z\overline{\beta}\left(-K_z\overline{\boldsymbol{w}}_{,y} - \overline{\beta}K_yK_z\overline{\boldsymbol{v}} + \overline{\beta}K_y^2\overline{\boldsymbol{w}}\right), \\ \boldsymbol{\xi}_{13}^B &= -z\overline{\beta}^2\overline{\boldsymbol{w}}, \\ \boldsymbol{\xi}_{21}^B &= -z\overline{\boldsymbol{w}}_{,yy}, \\ \boldsymbol{\xi}_{32}^B &= -z\overline{\beta}\left(2\overline{\boldsymbol{w}}_{,y} + 2\overline{\beta}K_z\overline{\boldsymbol{w}} - K_y\overline{\boldsymbol{u}}_{,y} + \overline{\beta}K_y\overline{\boldsymbol{v}} - \overline{\beta}K_yK_z\overline{\boldsymbol{u}}\right), \end{aligned} \tag{11}$$

$$
\begin{aligned}
\boldsymbol{\xi}_{xx11} &= \frac{\overline{\beta}^2}{2}\left(K_z^2\overline{\boldsymbol{v}\boldsymbol{v}}^T - 2K_yK_z\overline{\boldsymbol{v}\boldsymbol{w}}^T + K_y^2\overline{\boldsymbol{w}\boldsymbol{w}}^T\right),\\
\boldsymbol{\xi}_{xx22} &= \frac{\overline{\beta}^2}{2}\left(\frac{1}{R_C^2}\overline{\boldsymbol{u}\boldsymbol{u}}^T + \overline{\boldsymbol{v}\boldsymbol{v}}^T + \overline{\boldsymbol{w}\boldsymbol{w}}^T + 2K_z\overline{\boldsymbol{u}\boldsymbol{v}}^T - 2K_y\overline{\boldsymbol{u}\boldsymbol{w}}^T\right),\\
\boldsymbol{\xi}_{xx33} &= \frac{\overline{\beta}^2}{2}\overline{\boldsymbol{u}\boldsymbol{u}}^T,\\
\boldsymbol{\xi}_{xx31} &= \overline{\beta}^2\left(K_y\overline{\boldsymbol{u}\boldsymbol{w}}^T - K_z\overline{\boldsymbol{u}\boldsymbol{v}}^T\right),\\
\boldsymbol{\xi}_{yy11} &= \frac{1}{2}\left(\overline{\boldsymbol{v}}_{,y}\overline{\boldsymbol{v}}_{,y}^T + \overline{\boldsymbol{w}}_{,y}\overline{\boldsymbol{w}}_{,y}^T\right),\\
\boldsymbol{\xi}_{yy22} &= \frac{1}{2}\overline{\boldsymbol{u}}_{,y}\overline{\boldsymbol{u}}_{,y}^T,\\
\boldsymbol{\xi}_{xy21} &= \overline{\beta}\left(\overline{\boldsymbol{v}\boldsymbol{v}}_{,y}^T + \overline{\boldsymbol{w}\boldsymbol{w}}_{,y}^T - K_y\overline{\boldsymbol{u}\boldsymbol{w}}_{,y}^T + K_y\overline{\boldsymbol{u}}_{,y}\overline{\boldsymbol{w}}^T + K_z\overline{\boldsymbol{u}\boldsymbol{v}}_{,y}^T - K_z\overline{\boldsymbol{u}}_{,y}\overline{\boldsymbol{v}}^T\right),\\
\boldsymbol{\xi}_{xy32} &= \overline{\beta}\overline{\boldsymbol{u}\boldsymbol{u}}_{,y}^T,
\end{aligned}
\tag{12}
$$

where the omitted $\boldsymbol{\xi}_{ijkl}$ vectors are null.

The linear stability analysis eigenvalue equation reads, as usual, in Voigt notation,

$$
\int_L \int_A \delta\boldsymbol{\varepsilon}^T\boldsymbol{C}\Delta\boldsymbol{\varepsilon} + \lambda(\Delta\delta\boldsymbol{E}^M)^T\boldsymbol{S}^M\frac{R}{R_C}\,dA\;dX = 0, \tag{13}
$$

where δ denotes a virtual variation, Δ is a small configuration change to the post-buckling path, $(\boldsymbol{S}^M)^T = \begin{bmatrix} S_{xx}^M & S_{yy}^M & S_{xy}^M \end{bmatrix}$ are membrane pre-buckling second Piola-Kirchhoff stresses (the bending stresses can be discarded due to the thin walls), A is the cross-section area, L is the axis length and $\boldsymbol{C}$ is the constitutive matrix. Using the former equations and uncoupling the membrane and bending terms through $R/R_C \approx \overline{R}/R_C = 1/\overline{\beta}$, one is led to

$$
\int_L \delta\boldsymbol{\Phi}^T\left(\int_A \frac{1}{\overline{\beta}}\left((\boldsymbol{\Xi}_{\boldsymbol{\varepsilon}}^M)^T\boldsymbol{C}^M\boldsymbol{\Xi}_{\boldsymbol{\varepsilon}}^M + (\boldsymbol{\Xi}_{\boldsymbol{\varepsilon}}^B)^T\boldsymbol{C}^B\boldsymbol{\Xi}_{\boldsymbol{\varepsilon}}^B + \lambda\boldsymbol{\Theta}_{D^2\boldsymbol{E}}(\boldsymbol{S}^M)\right)dA\right)\,\Delta\boldsymbol{\Phi}\,dX = 0, \tag{14}
$$

where the geometric or initial stress matrix is given by $\boldsymbol{\Theta}_{D^2\boldsymbol{E}}(\boldsymbol{S}^M) = S_{xx}^M\boldsymbol{\Theta}_{xx} + S_{yy}^M\boldsymbol{\Theta}_{yy} + S_{xy}^M\boldsymbol{\Theta}_{xy}$, with $\boldsymbol{\Theta}_{ij} = \boldsymbol{\Xi}_{ij}^{M,NL} + \left(\boldsymbol{\Xi}_{ij}^{M,NL}\right)^T$, and the constitutive matrices for a St. Venant-Kirchhoff material law and plane stress read

$$
\boldsymbol{C}^B = \boldsymbol{C}^M = \begin{bmatrix} \frac{E}{1-\nu^2} & \frac{\nu E}{1-\nu^2} & 0 \\ \frac{\nu E}{1-\nu^2} & \frac{E}{1-\nu^2} & 0 \\ 0 & 0 & G \end{bmatrix}, \tag{15}
$$

where E is Young's modulus, ν is Poisson's ratio and G is the shear modulus. If it is assumed that $\varepsilon_{yy}^M = 0$, which is acceptable in a wide range of cases and leads to significant computational savings, one adopts instead

$$\boldsymbol{C}^M = \begin{bmatrix} E & 0 & 0 \\ 0 & 0 & 0 \\ 0 & 0 & G \end{bmatrix}, \tag{16}$$

to avoid an over-stiffness effect due to unrelieved Poisson effects.

3. Deformation modes

The linear part of Eq. (13) can be written as

$$\int_L \delta\boldsymbol{\Phi}^T \begin{bmatrix} \mathbf{B}+\mathbf{E}+\mathbf{E}^T+\mathbf{G} & \mathbf{0} & \mathbf{D}_2+\mathbf{F} \\ \mathbf{0} & \mathbf{D}_1 & \mathbf{0} \\ (\mathbf{D}_2+\mathbf{F})^T & \mathbf{0} & \mathbf{C} \end{bmatrix} \boldsymbol{\Phi}\, dX, \tag{17}$$

$$\begin{aligned} &\mathbf{B} = \int_A \tfrac{E}{1-\nu^2}\tfrac{R}{R_C}\,\boldsymbol{\xi}_{21}\boldsymbol{\xi}_{21}^T dA, && \mathbf{C} = \int_A \tfrac{E}{1-\nu^2}\tfrac{R}{R_C}\,\boldsymbol{\xi}_{13}\boldsymbol{\xi}_{13}^T dA, \\ &\mathbf{D}_1 = \int_A \tfrac{GR}{R_C}\,\boldsymbol{\xi}_{32}\boldsymbol{\xi}_{32}^T dA, && \mathbf{D}_2 = \int_A \tfrac{\nu E}{1-\nu^2}\tfrac{R}{R_C}\,\boldsymbol{\xi}_{21}\boldsymbol{\xi}_{13}^T dA, \\ &\mathbf{E} = \int_A \tfrac{\nu E}{1-\nu^2}\tfrac{R}{R_C}\,\boldsymbol{\xi}_{11}\boldsymbol{\xi}_{21}^T dA, && \mathbf{F} = \int_A \tfrac{E}{1-\nu^2}\tfrac{R}{R_C}\,\boldsymbol{\xi}_{11}\boldsymbol{\xi}_{13}^T dA, \\ &\mathbf{G} = \int_A \tfrac{E}{1-\nu^2}\tfrac{R}{R_C}\,\boldsymbol{\xi}_{11}\boldsymbol{\xi}_{11}^T dA, \end{aligned} \tag{18}$$

where **B**, **C**, **D**, **E**, **F** and **G** correspond to the cross-section integration of the cross-section deformation mode functions ($\overline{u}_k$, $\overline{v}_k$ and $\overline{w}_k$) and are designated as "GBT modal matrices". It should be noted that matrices **E**, **F** and **G** are null for prismatic members.

The cross-section deformation modes are obtained with the help of the GBT modal matrices, by taking the following steps (Fig. 2 shows an example):

1. The cross-section is discretized using (i) "natural" nodes, located at wall mid-line intersections and free edges, and (ii) "intermediate" nodes, arbitrarily placed along the wall mid-lines, between natural nodes, to refine the discretization. In Fig. 2(a), six natural nodes and one intermediate node are defined (7 nodes).
2. An initial basis for the deformation modes is generated from the three translational DOFs at each node (rotations are statically condensed) and using Hermite cubic functions for $\overline{w}_k$, while linear functions for $\overline{u}_k$ and $\overline{v}_k$. In Fig. 2(b), 3 DOFs per each of the 7 nodes leads to the 21 initial modes shown.
3. The final deformation modes are obtained from the initial basis through several change of basis operations, using the eigenvectors of the GBT modal matrices:
   3.1 The eigenvectors of $\mathbf{B}^M$ are used to separate the deformation modes into $\mathbf{B}^M$-orthogonal transverse extension modes ($\lambda \neq 0$, modes 16 to 21 in Fig. 2(c)) and transverse inextensible modes ($\lambda = 0$), which need to be further processed, as discussed next.
   3.2 In the transverse inextensible mode space, the eigenvectors of $\mathbf{D}_1^M$ are employed to subdivide the modes into shear ($\lambda \neq 0$) and Vlasov/local-plate ($\lambda = 0$) modes. Each subset is then treated separately, as explained next.
   3.3 The Vlasov and local-plate modes are hierarchized by solving the generalized eigenvalue problem

$$\left(\mathbf{B}^B - \lambda\mathbf{C}\right)\boldsymbol{v} = \mathbf{0}. \tag{19}$$

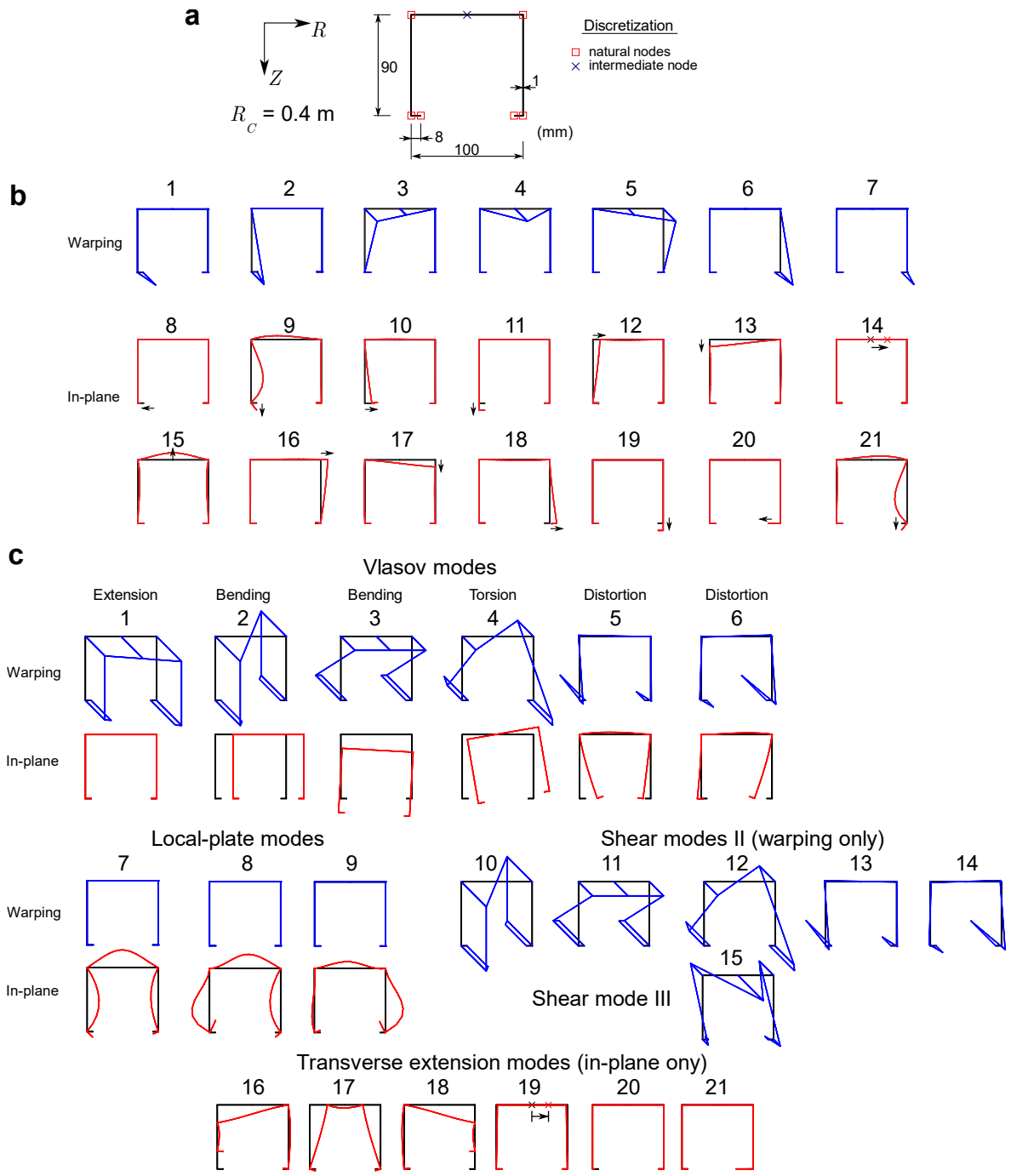

Figure 2: (a) lipped channel geometry and discretization, (b) initial and (c) final deformation modes

The $\lambda \neq 0$ eigenvectors define the final distortional and local-plate modes (modes 5-9 in Fig. 2(c)). The $\lambda = 0$ eigenvectors constitute a basis of the "rigid-body" modes, which are trivially defined as axial extension (tangential displacements), in-plane bending (radial) and out-of-plane bending (modes 1-3 in Fig. 2(c)) plus a torsion mode for open sections which corresponds to the $\lambda \neq 0$ eigenvector in this 4D subspace of

$$\left(\mathbf{D}_1^B - \lambda \mathbf{C}^M\right)\boldsymbol{v} = \mathbf{0}, \tag{20}$$

since the nullspace of $\mathbf{D}_1^B$ corresponds to the first three modes and $\mathbf{C}^M$ ensures orthogonality of the warping functions.

3.4 The shear modes are subdivided into (I) cell shear flow modes for closed sections, (II) warping functions of the bending, torsion (for open sections only) and distortional modes (modes 10-14 in Fig. 2(c)), and (III) additional warping functions (mode 15 in Fig. 2(c)). The III modes are obtained as the $\mathbf{C}^M$-orthogonal complement of the II modes plus mode 1, which is subsequently orthogonalized and hierarchized using the eigenvectors of

$$\left(\mathbf{D}_1^M - \lambda \mathbf{C}^M\right)\boldsymbol{v} = \mathbf{0}. \tag{21}$$

For the I modes, a basis for the mode space of independent $\overline{v}$ displacements is obtained and added to the II and III shear modes, excluding the warping functions of modes 2 and 3. Then, one solves

$$\left(\mathbf{B}^B - \lambda\left(\mathbf{B}^B + \mathbf{D}_1^M\right)\right)\boldsymbol{v} = \mathbf{0}, \tag{22}$$

since the $0 < \lambda < 1$ eigenvectors correspond to the desired space excluding torsion. The torsional mode is obtained from the $\lambda = 0$ eigenvector space, by calculating the eigenvector of the single non-null eigenvalue of

$$\left(\mathbf{D}_1^B - \lambda \mathbf{D}_1^M\right)\boldsymbol{v} = \mathbf{0}. \tag{23}$$

The previous procedure retrieves linear transverse extension modes (linear $\overline{v}_k$ functions), which can be insufficient to capture the pre-buckling membrane radial stresses in curved members, as discussed in section 5. This can be effectively solved by adding "quadratic" transverse extension modes (quadratic $\overline{v}_k$ functions), each corresponding to a "bubble" function between consecutive cross-section nodes (wall segment).

4. Finite element formulation

As usual, a GBT-based finite element can be obtained by approximating the amplitude functions $\phi_k(X)$ by means of Hermite cubic polynomials except for the deformation modes that only involve warping, in which case Lagrange quadratic functions are used (Gonçalves & Camotim 2011, 2012). Formally, one writes

$$\boldsymbol{\Phi} = \boldsymbol{\Psi}\boldsymbol{d}_e, \quad \boldsymbol{\Psi} = \begin{bmatrix} \boldsymbol{\psi} \\ \boldsymbol{\psi}' \\ \boldsymbol{\psi}'' \end{bmatrix} \tag{24}$$

where vector $\boldsymbol{d}_e$ collects the element DOFs and matrix $\boldsymbol{\psi}$ groups the approximation functions. Substituting the approximation in Eq. (14) leads to the element linear and geometric stiffness matrices

$$\boldsymbol{K}_e = \int_L \boldsymbol{\Psi}^T \int_A \frac{1}{\bar{\beta}} ((\boldsymbol{\Xi}_{\boldsymbol{\varepsilon}}^M)^T \boldsymbol{C}^M \boldsymbol{\Xi}_{\boldsymbol{\varepsilon}}^M + (\boldsymbol{\Xi}_{\boldsymbol{\varepsilon}}^B)^T \boldsymbol{C}^B \boldsymbol{\Xi}_{\boldsymbol{\varepsilon}}^B)\, dA\ \boldsymbol{\Psi}\, dX,$$
$$\boldsymbol{G}_e = \int_L \boldsymbol{\Psi}^T \int_A \frac{1}{\bar{\beta}} \boldsymbol{\Theta}_{D^2 \boldsymbol{E}}(\boldsymbol{S}^M)\, dA\, \boldsymbol{\Psi}\, dX. \tag{25}$$

These matrices are calculated using (i) 3 Gauss points along X (reduced scheme to avoid membrane locking in curved members), (ii) 3 Gauss points along y between consecutive cross-section nodes, which suffices in the examples presented next, and (iii) analytical integration in the through-thickness direction z.

A linear stability analysis requires a preliminary linear step to obtain the pre-buckling stresses,

$$\boldsymbol{K}\boldsymbol{d} = \boldsymbol{f} \tag{26}$$

where $\boldsymbol{K}$ and $\boldsymbol{d}$ are assembled from all $\boldsymbol{K}_e$ and $\boldsymbol{d}_e$, respectively, while $\boldsymbol{f}$ is the external load vector. The bifurcation problem further requires the assembly of all element geometric stiffness matrices $\boldsymbol{G}_e$ into matrix $\boldsymbol{G}$ and solving the eigenvalue problem

$$(\boldsymbol{K} + \lambda \boldsymbol{G})\Delta \boldsymbol{d} = \boldsymbol{0}, \tag{27}$$

where the eigenvalues λ are the bifurcation load parameter values and the eigenvectors $\Delta \boldsymbol{d}$ define the associated buckling modes.

It is worth remarking that the GBT-based finite element procedure is quite fast. The authors have implemented the procedure in MATLAB (The MathWorks Inc. 2018) and, for the example in Section 5.1 with 43 deformation modes and 30 finite elements (≈2600 DOFs), the complete analysis takes only about 2 seconds.

5. Numerical examples

In all examples presented next, the material parameters adopted are $E = 210$ GPa and $\nu = 0.3$, the loads are given in kN and the cross-section center C coincides with the centroid. For comparison purposes, results obtained with refined meshes of shell finite elements are presented, using ADINA (Bathe 2019). The relative percentage difference between the GBT-based and shell element models is calculated as $\Delta = 100 \times (\mathrm{f}_{GBT} - \mathrm{f}_{shell})/\mathrm{f}_{shell}$, where f is the value compared.

5.1 90º lipped channel cantilever

The first example concerns the 90º cantilever shown in Fig. 3(a). The cross-section discretization adopted leads to the 13 Vlasov modes depicted in Fig. 3(b), plus 10 shear, 10 linear transverse extension and 10 quadratic transverse extension modes.

Curved members may require a shell finite element mesh which is much more refined than what is typically necessary for straight members. To illustrate this point, Table 1 displays the first four bifurcation loads obtained with two meshes (1840/6656 elements, corresponding to 0.04/0.02 element widths) of 4-node (bilinear) and 9-node (quadratic) MITC (Mixed Interpolation of Tensorial Components) shell elements. Clearly, 1840 MITC9 elements suffice, as halving the

element widths leads to differences below 0.03%, but none of the MITC4 models yields acceptable results. Consequently, only MITC9 elements are employed in the subsequent analyses.

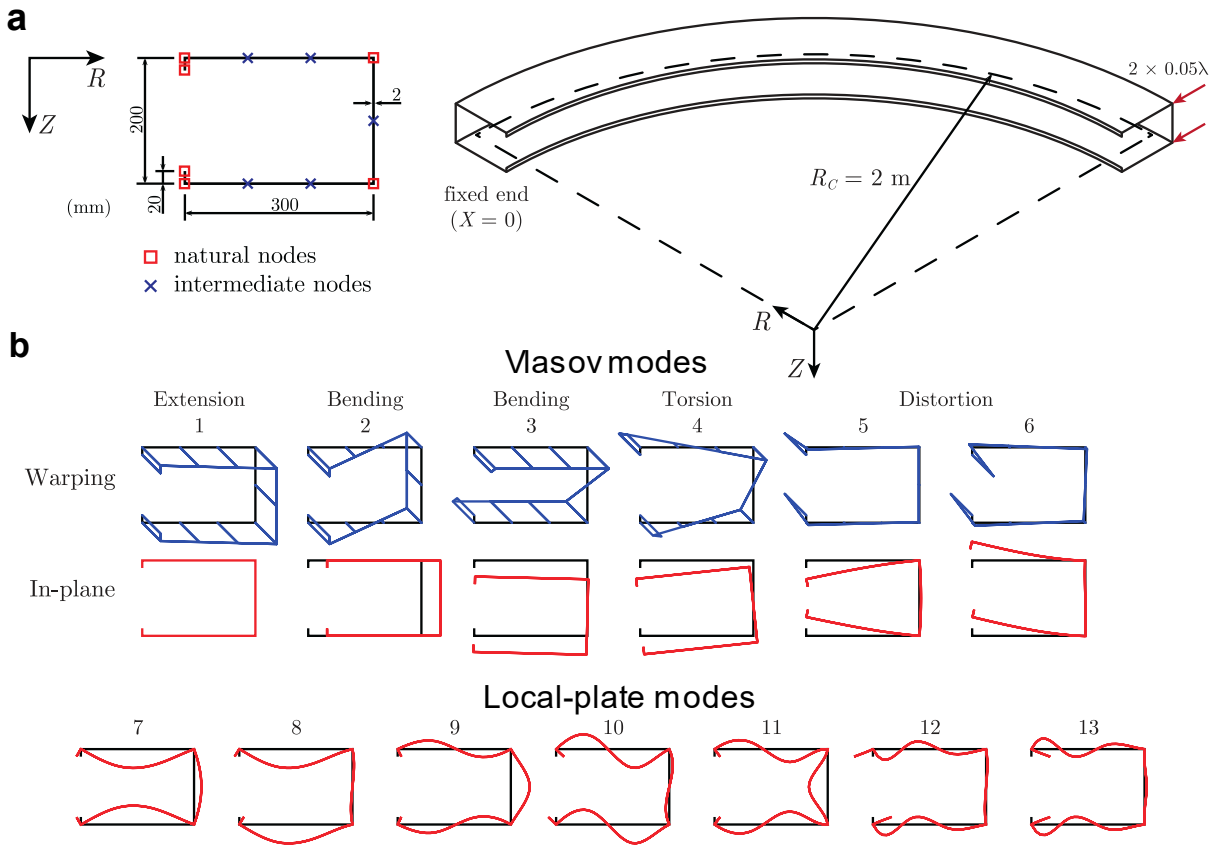

Figure 3: 90º lipped channel arch: (a) geometry, loading, boundary conditions, GBT cross-section discretization, and (b) Vlasov and local-plate deformation modes

Table 1: Lipped channel cantilever: first four bifurcation load parameter values

Mode	1840 MITC4 (9920 DOFs)	6656 MITC4 (34495 DOFs)	1840 MITC9 (38240 DOFs)	6656 MITC9 (135310 DOFs)
1	43.60	39.35	36.92	36.91
2	43.77	39.60	37.19	37.19
3	57.61	51.78	48.26	48.25
4	58.29	52.15	48.51	48.50

Table 2 provides the first four bifurcation loads obtained using the proposed GBT-based finite element, using several discretizations and deformation mode sets, and the differences with respect to the 1840 MITC9 shell element model. It is observed that the GBT results converge for 10 elements (differences with respect to the values for 30 elements below 1%), but the linear transverse extension modes must be included in the analysis, as Δ decreases in some cases from more than 50% to about 3%, which shows that the pre-buckling membrane radial stresses influence considerably the results. These radial stresses are compressive if the bending moment increases the curvature (the present case) and therefore produce a destabilizing effect. Adding quadratic transverse extension modes further improves the results, but to a much lesser extent. It should be remarked that the GBT approach involves much less DOFs than the shell model. For instance, with

all deformation modes one has only 860/2580 DOFs for 10/30 GBT-based elements, respectively, whereas the shell model involves 38240 DOFs.

Table 2: Lipped channel cantilever: first four GBT-based bifurcation loads and differences with respect to the 1840 MITC9 shell model

Vlasov + local-plate + shear deformation modes

Mode	10 FE		20 FE		30 FE	
	λ	Δ	λ	Δ	λ	Δ
1	58.2	-58%	58.0	-57%	58.0	-57%
2	57.1	-53%	56.9	-53%	56.9	-53%
3	63.9	-32%	63.5	-32%	63.5	-32%
4	64.1	-32%	63.8	-31%	63.7	-31%
Vlasov + local-plate + shear + linear transverse extension deformation modes						
1	35.9	2.7%	35.8	3.1%	35.7	3.2%
2	36.2	2.6%	36.1	3.0%	36.1	3.0%
3	49.4	-2.4%	49.1	-1.8%	49.1	-1.8%
4	49.8	-2.7%	49.5	-2.1%	49.5	-2.0%
All modes						
1	37.5	-1.5%	37.3	-1.0%	37.3	-1.0%
2	37.9	-2.0%	37.8	-1.6%	37.7	-1.5%
3	49.3	-2.2%	49.0	-1.6%	49.0	-1.5%
4	49.4	-1.8%	49.0	-1.1%	49.0	-1.0%

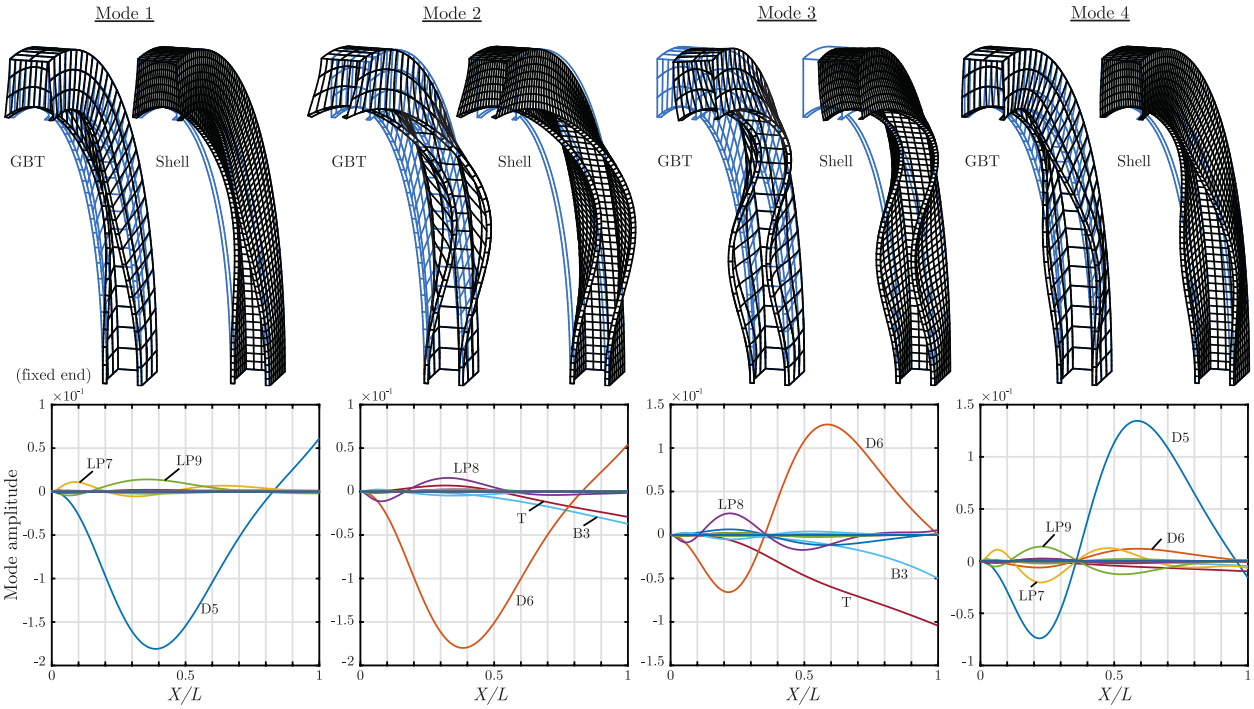

Figure 4: Lipped channel cantilever: first four buckling modes and deformation mode amplitude graphs

Fig. 4 shows the first four buckling modes obtained with the shell and GBT models, as well as the corresponding GBT deformation mode amplitude function graphs. An almost perfect agreement between the buckling modes is observed, despite their complexity and the significant difference in terms of DOF numbers associated with each model. Furthermore, the mode amplitude graphs show

that: (i) the first buckling mode is symmetric distortional (D5), with small contributions of two local-plate modes (LP7+9), (ii) the second buckling mode involves anti-symmetric distortion (D6), out-of-plane bending (B3), torsion (T) and one local-plate mode (LP8), and (iii) the third/fourth buckling modes are higher-order versions of the second/first mode, respectively.

5.2 90º I-section cantilever

In this example the 90º I-section cantilevered arch shown in Fig. 5(a) is analyzed. The cross-section discretization originates 43 deformation modes (Fig. 5(b)): 4 rigid-body, 9 local-plate, 10 shear, 10 linear transverse extension and 10 quadratic transverse extension. All GBT results presented next are obtained with 30 elements and all deformation modes, amounting to 2580 DOFs. Results obtained with a refined MITC9 shell model (0.03 m element width, 2700 elements, 55400 DOFs) are presented for comparison purposes. The results are presented in Table 3 and Fig. 6.

The values in Table 3 show that there is an excellent agreement between the bifurcation loads obtained with both models, since the differences are below 1.4% despite the huge difference in terms of DOF numbers (2580/55400 for the GBT/shell models, respectively). The buckling mode shapes in Fig. 6 further confirm the agreement. Finally, the deformation mode amplitude function graphs make it possible to conclude that modes 1/2 and 3/4 are similar — the latter are higher-order versions of the former —, involving essentially the local-plate deformation modes 5+7 (symmetric local buckling) and 6+8 (anti-symmetric local buckling), respectively.

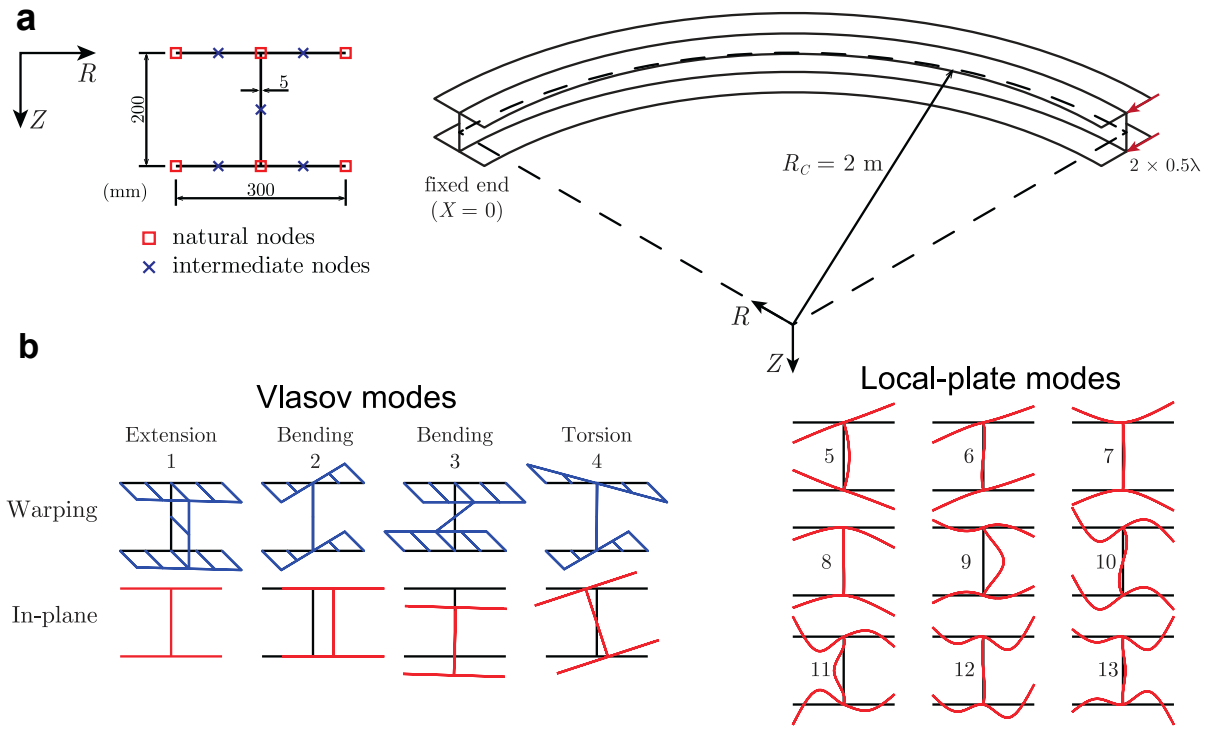

Figure 5: 90º I-section arch: (a) geometry, loading, boundary conditions, GBT cross-section discretization, and (b) Vlasov and local-plate deformation modes

Table 3: I-section cantilever: first four GBT-based bifurcation loads and differences with respect to the shell model

Mode	Shell	GBT	Δ
1	22.25	22.54	1.3%
2	22.52	22.82	1.3%
3	23.01	23.33	1.4%
4	23.30	23.62	1.4%

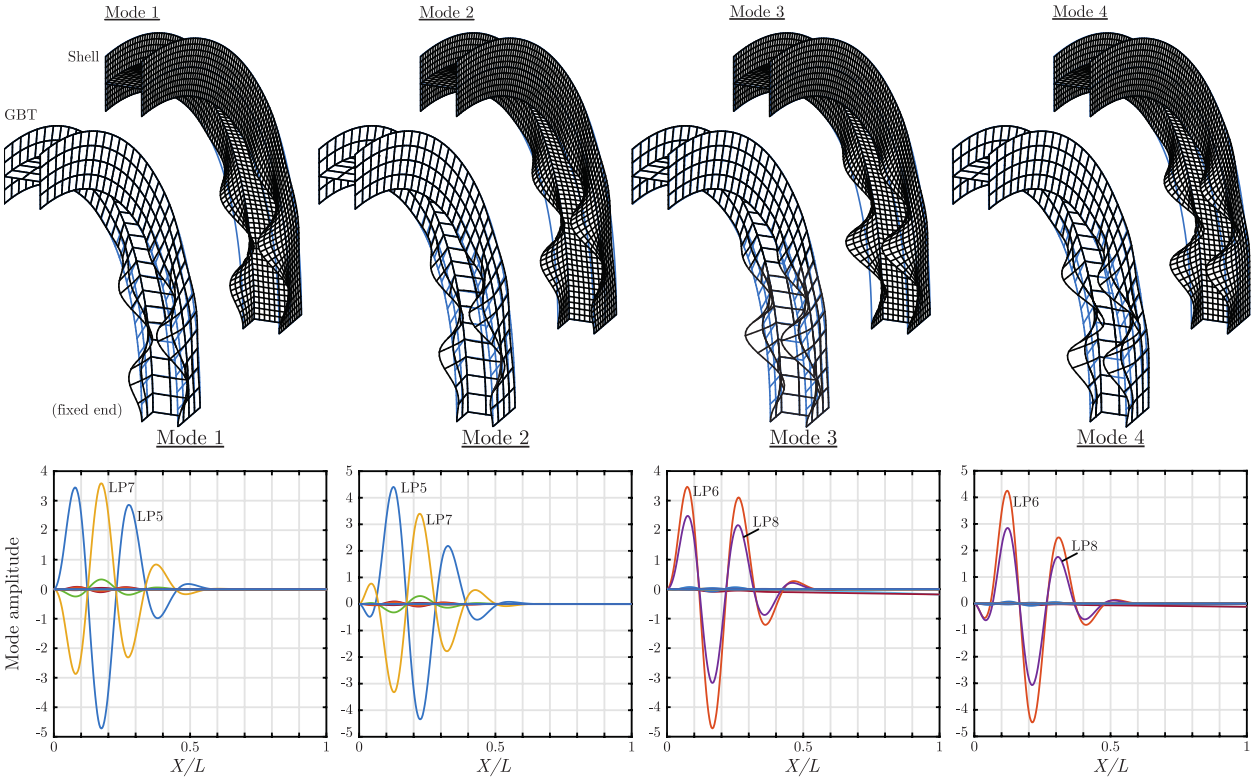

Figure 6: I-section cantilever: first four buckling modes and deformation mode amplitude graphs

5.3 180º I-section arch

Finally, the 180º fixed-fixed I-section arch shown in Fig. 7(a) is analyzed. The cross-section discretization adopted leads to 47 deformation modes (Fig. 7(b)): 4 rigid-body, 10 local-plate, 11 shear, 11 linear transverse extension and 11 quadratic transverse extension. In this case the MITC9 shell model has 0.025 m element width, amounting to 5760 elements and 118313 DOFs. Only the first two bifurcation loads and buckling modes are presented, since the next two are once more only higher-order versions.

Table 4 provides the first two bifurcation load parameters for several GBT discretizations (all deformation modes are included; only the number of elements is varied). The first bifurcation load is adequately estimated using 30 elements, as in previous examples, but the second bifurcation load requires at least 50 elements (this is explained next).

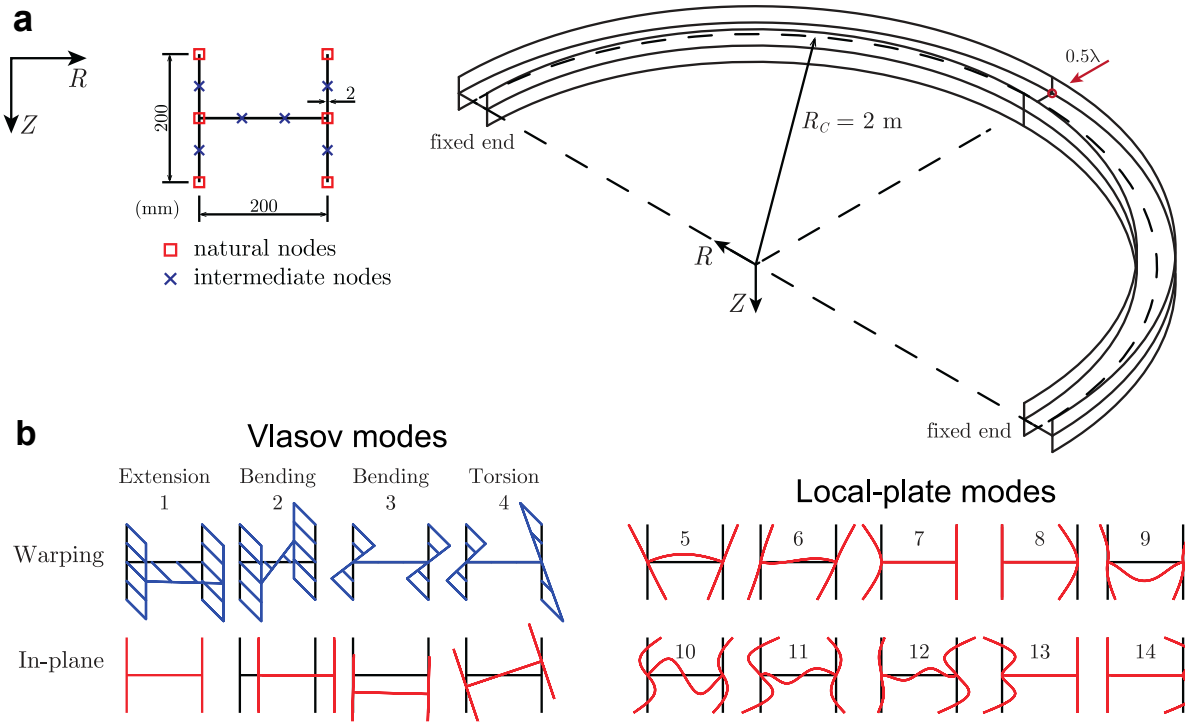

Figure 7: 180º I-section arch: (a) geometry, loading, boundary conditions, GBT cross-section discretization and (b) Vlasov and local-plate deformation modes

Table 4: 180º I-section arch: first two bifurcation load parameters and differences with respect to the shell model

Mode	Shell	GBT (30 FE, 2738 DOFs)	Δ	GBT (50 FE, 4618 DOFs)	Δ	GBT (100 FE, 9318 DOFs)	Δ
1	10.12	10.27	1.5%	10.17	0.5%	10.13	0.1%
2	54.78	61.82	12.9%	57.33	4.7%	56.21	2.6%

The buckling modes and the corresponding GBT deformation mode amplitude graphs are shown in Fig. 8, where the GBT results correspond to a model with 100 finite elements. Once again, a virtually perfect agreement is observed between the GBT-based and shell-based buckling modes. The mode amplitude graphs show that both buckling modes involve a major participation from the lateral bending (B3) and torsion (T) rigid-body modes. However, while the first mode is essentially lateral-torsional, the second one involves an additional significant participation of two LP deformation modes (LP5+6), particularly near the point of load application, thus explaining the need to use at least 50 GBT-based finite elements to obtain accurate results.

6. Concluding remarks

This paper presented and validated a GBT-based finite element able to perform buckling (linear stability) analyses of thin-walled members with circular axis, accounting for global-distortional-local deformation. Although the kinematics of curved members are quite involved, it was possible to (i) incorporate the classic GBT kinematic assumptions, which are essential to obtain significant computational savings with respect to shell finite element models, without sacrificing accuracy, and (ii) present all expressions required to implement the finite element in a simple vector-matrix form. The numerical examples presented in the paper show clearly that the proposed element produces very accurate results with a significant DOF economy with respect to a shell finite

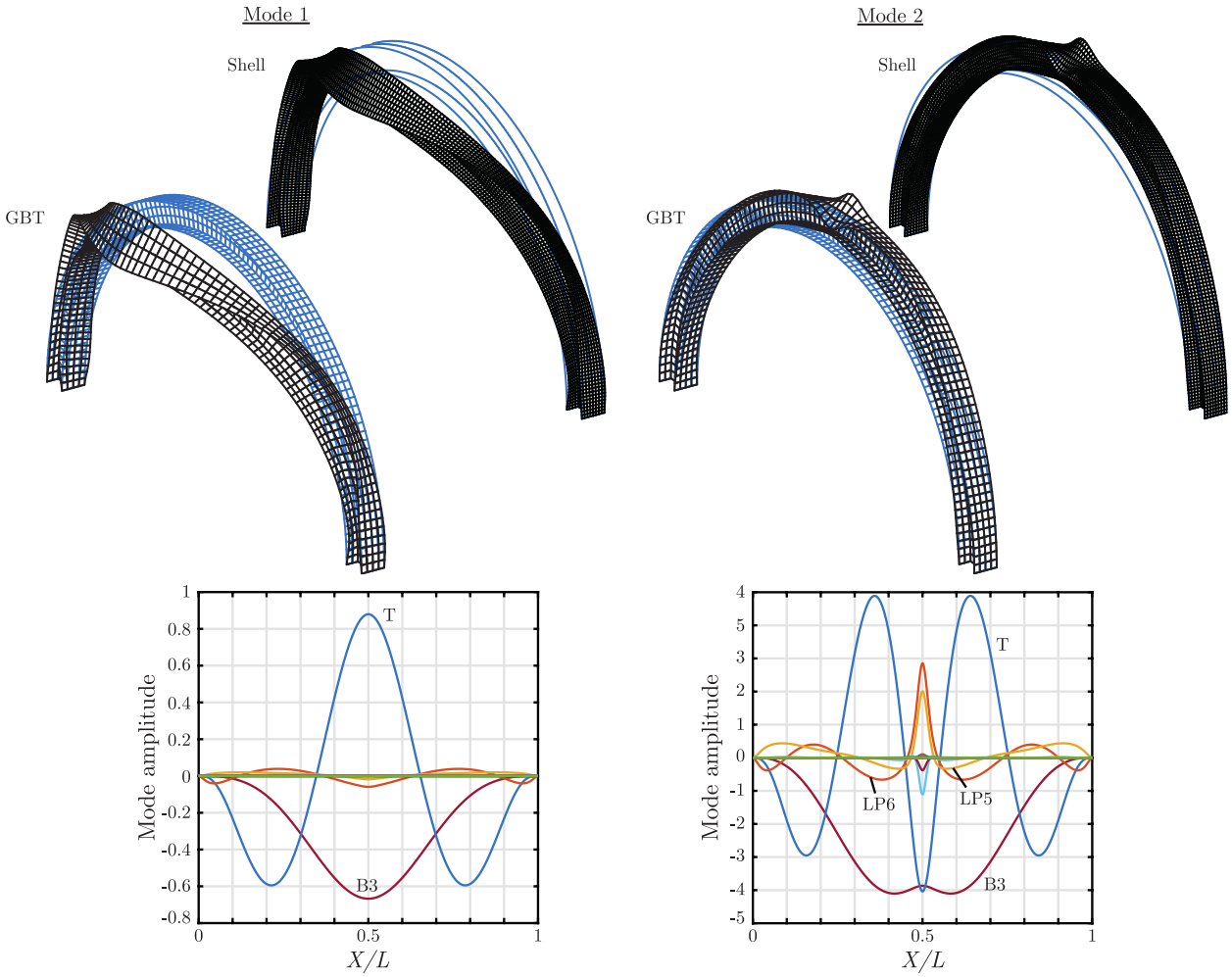

Figure 8: 180º I-section arch: first two buckling modes and deformation mode amplitude graphs

element model and that the GBT modal decomposition features can provide invaluable information concerning the nature of the buckling modes in curved members.

It is also worth remarking that, as shown in the paper, an accurate calculation of global-distortional-local bifurcation loads of curved thin-walled members requires (i) a shell finite element mesh much more refined than that usually required for prismatic members and (ii) the consideration of the membrane radial stresses, which in the GBT approach requires including membrane transverse extension modes.

Acknowledgment
The authors are grateful for the Foundation for Science and Technology's (FCT, Portugal) support through funding UIDB/04625/2020 from the research unit CERIS.

References
Bathe, K. (2019). *ADINA System*, ADINA R&D Inc.

Camotim, D., Basaglia, C., Bebiano, R., Gonçalves, R., Silvestre, N. (2010). "Latest developments in the GBT analysis of thin-walled steel structures." *Proceedings of the International Colloquium on Stability and Ductility of Steel Structures*, Rio de Janeiro, Brazil, 33-58.

Gonçalves, R, Ritto-Corrêa, M, Camotim, D. (2010). "A new approach to the calculation of cross-section deformation modes in the framework of Generalized Beam Theory." *Computational Mechanics*, 46 (5), 759-781.

Gonçalves, R., Camotim, D. (2011). "Generalised Beam Theory-based finite elements for elastoplastic thin-walled metal members." *Thin-Walled Structures*, 49 (10), 1237-1245.

Gonçalves, R., Camotim, D. (2012). "Geometrically non-linear Generalised Beam Theory for elastoplastic thin-walled metal members." *Thin-Walled Structures*, 51, 121-129.

Gonçalves, R, Bebiano, R, Camotim, D. (2014). "On the shear deformation modes in the framework of Generalized Beam Theory." *Thin-Walled Structures*, 84, 325-334.

Habtemariam, A., Könke, C., Zabel, V., Bianco, M. (2021a). "Generalized Beam Theory formulation for thin-walled pipes with circular axis." *Thin-Walled Structures*, 159, 107243.

Habtemariam, A., Tartaglione, F., Zabel, V., Könke, C., Bianco, M. (2021b). "Vibration analysis of thin-walled pipes with circular axis using the generalized beam theory." *Thin-Walled Structures*, 163, 107628.

Habtemariam, A., Bianco, M., Könke, C., Zabel, V. (2022). "Geometrically nonlinear formulation of Generalized Beam Theory for the analysis of thin-walled circular pipes." *Thin-Walled Structures*, 173, 109029.

Peres, N., Gonçalves, R., Camotim, D. (2016). "First-order Generalised Beam Theory for curved thin-walled members with circular axis." *Thin-Walled Structures*, 107, 345-361.

Peres, N., Gonçalves, R., Camotim, D. (2018). "GBT-based cross-section deformation modes for curved thin-walled members with circular axis." *Thin-Walled Structures*, 127, 769-780.

Peres, N., Gonçalves, R., Camotim, D. (2020). "A GBT-based mixed finite element for curved thin-walled members with circular axis." *Thin-Walled Structures*, 146, 106462.

Peres, N., Gonçalves, R., Camotim, D. (2022a). "GBT-based dynamic analysis of thin-walled members with circular axis." *Thin-Walled Structures*, 170, 108533.

Peres, N., Gonçalves, R., Camotim, D. (2022b). "Generalised Beam Theory formulation for the buckling analysis of thin-walled members with circular axis." *Thin-Walled Structures*, 176, 109322.

Schardt, R. (1989). *Verallgemeinerte Technische Biegetheorie*, Berlin, Springer Verlag.

The MathWorks Inc. (2018). *MATLAB R2018a*, Massachusetts.